

Dynamics of topological defects after a photo-induced melting of a charge-density wave

Andrei E. Tarkhov,^{1,2,3} A.V. Rozhkov,^{1,4} Alfred Zong,^{5,6} Anshul Kogar,⁵ Nuh Gedik,⁵ and Boris V. Fine^{1,3,7}

¹Laboratory for the Physics of Complex Quantum Systems, Moscow Institute of Physics and Technology, Institutskiy per. 9, Dolgoprudny, Moscow region, 141700, Russia

²Division of Genetics, Department of Medicine, Brigham and Women's Hospital and Harvard Medical School, Boston, MA 02115, USA

³Skolkovo Institute of Science and Technology, Bolshoy Boulevard 30, bld. 1, Moscow, Russia, 121205*

⁴Institute for Theoretical and Applied Electrodynamics, Russian Academy of Sciences, Moscow 125412, Russia

⁵Massachusetts Institute of Technology, Department of Physics, Cambridge, MA 02139, USA

⁶University of California at Berkeley, Department of Chemistry, Berkeley, CA, 94720, USA

⁷Institute for Theoretical Physics, University of Leipzig, Brüderstrasse 16, 04103 Leipzig, Germany[†]

(Dated: March 11, 2022)

Charge-density-wave order in a solid can be temporarily “melted” by a strong laser pulse. Here we use the discrete Gross-Pitaevskii equation on a cubic lattice to simulate the recovery of the CDW long-range phase coherence following such a pulse. Our simulations indicate that the recovery process is dramatically slowed down by the three-dimensional topological defects – CDW dislocations – created as a result of strongly nonequilibrium heating and cooling of the system. Overall, the simulated CDW recovery was found to be strongly reminiscent of a recent pump-probe experiment in LaTe_3 .

Topological defects in the form of vortices play a prominent role in nonequilibrium and equilibrium statistical physics of ordered systems [1–13]. In particular, vortices are known to emerge through the Kibble-Zurek mechanism [14–17], when the system is cooled across a phase transition. In the Kibble-Zurek setting, the system is initially at equilibrium, and the cooling process is supposed to be adiabatic everywhere except for a close vicinity of the phase transition temperature. It is still an outstanding question: What happens after a quench across a phase transition, where the initial state is far from equilibrium, and the energy flow from the system is so fast that the system does not reach quasi-equilibrium at any time during the quench?

In the present work, we address the above question in the context of the recent pump-probe experiment of Ref. [18] on the light-induced melting of a charge-density wave (CDW) in LaTe_3 . The experiment monitored the recovery of the CDW order after its destruction by a laser pulse. The experimental system was initially in the low-temperature ordered phase; then the part of the system responsible for the CDW order was rapidly heated up and cooled down, so that it did not have time to reach the high-temperature equilibrium. It was observed [18] that the amplitude and the phase of the CDW after photo-excitation behaved qualitatively differently: the amplitude recovered quickly, whereas, for sufficiently high pump pulse intensity, the recovery of phase coherence took much longer times [19]. It was conjectured in Ref. [18] on the basis of indirect experimental evidence that the observed slowdown of the CDW-order recovery is due to the slow dynamics of the photoinduced topological defects – CDW dislocations. Topological defects

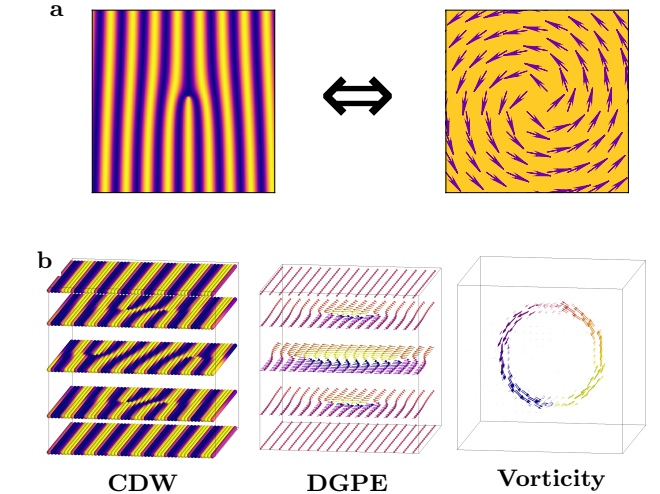


FIG. 1. Sketch of the mapping of a CDW dislocation $u \cos[\mathbf{q}_{\text{CDW}}\mathbf{r}_m + \phi(\mathbf{r}_m)]$ onto a vortex of the DGPE $U(1)$ lattice variables $u \exp[i\phi(\mathbf{r}_m)]$. (a) 2D slice of the CDW dislocation (left) vs. 2D slice of the DGPE vortex (right). (b) Three-dimensional representations of a vortex loop: CDW (left) vs. DGPE lattice (middle) vs. vorticity of the DGPE lattice defined in the text (right).

within the CDW phase were also invoked in other contexts in Refs. [20–27].

The translational symmetry breaking associated with the onset of a CDW can be equivalently viewed as the breaking of the $U(1)$ symmetry with respect to the phase of the CDW order parameter. In such a picture, the CDW dislocations are mapped onto vortices in the underlying $U(1)$ -ordered state (see Fig. 1).

In the present work, we simulate the principal features of the CDW phase dynamics with the help of the discrete Gross-Pitaevskii equation (DGPE), which also exhibits a $U(1)$ phase transition. We implement the heating-cooling quench, perform the numerical imaging of vortices, trace their dynamics and, thereby demonstrate that they are responsible for the slowdown of the order parameter recovery. The basic character of our simulations suggest that the observed non-equilibrium phenomenology is broadly universal, and can be searched for in other physical systems as well.

General considerations. — CDW is a modulation of electronic charge density accompanied by a periodic modulation of ionic positions

$$\mathbf{r}_m \rightarrow \mathbf{r}_m + u \mathbf{e} \cos(\mathbf{q}_{\text{CDW}} \mathbf{r}_m + \phi), \quad (1)$$

where \mathbf{r}_m is the position of the m 'th ion, \mathbf{q}_{CDW} the CDW wave vector, u and ϕ the amplitude and the phase of the CDW, and \mathbf{e} the unit vector along the CDW lattice displacement direction [19]. One can choose the complex number $u \exp(i\phi)$ as the CDW order parameter. By allowing this order parameter to vary slowly in space and time, $u(\mathbf{r}, t) \exp(i\phi(\mathbf{r}, t))$, one can then describe the low-frequency dynamics of a CDW.

In Fig. 2(a), we reproduce one of the experimental results of Ref. [18], namely, the time dependence of the 2D-integrated intensity of the CDW diffraction peak for different fluences of the laser pump pulse. This intensity is proportional to the squared amplitude of the CDW order parameter. For smaller pulse fluences, the CDW order parameter initially becomes smaller but never vanishes entirely and then quickly recovers to almost the initial value. For higher fluences, the CDW first disappears, i.e. becomes totally melted, but then it recovers over much longer times, in fact, not reaching the equilibrium value on the timescale accessible in the experiment. The subsequent theoretical analysis of Ref. [19] concluded that the above slow recovery cannot be explained by the amplitude dynamics of the CDW order (see also [28, 29]). Both experiment [18] and theory [19] indicate that it takes time about 2 ps for the CDW amplitude to relax.

It is the phase relaxation happening afterwards that we aim at describing in this paper.

The model. — Our numerical model, DGPE, is a space-discretized version of the continuous Gross-Pitaevskii equation (GPE). Both can be considered as possible dynamical extensions of the static XY-model. The GPE describes the low-temperature dynamics of superfluid Bose gases, while the DGPE is often used to describe bosons on optical lattices. We note that both the spatially inhomogeneous CDW order $u(\mathbf{r}) \exp(i\phi(\mathbf{r}))$ and the DGPE share the $U(1)$ structure of the dynamical variable. The actual dynamics of the inhomogeneous CDW is different and, in many respects, more complex than that of DGPE. In particular, the latter is the case of

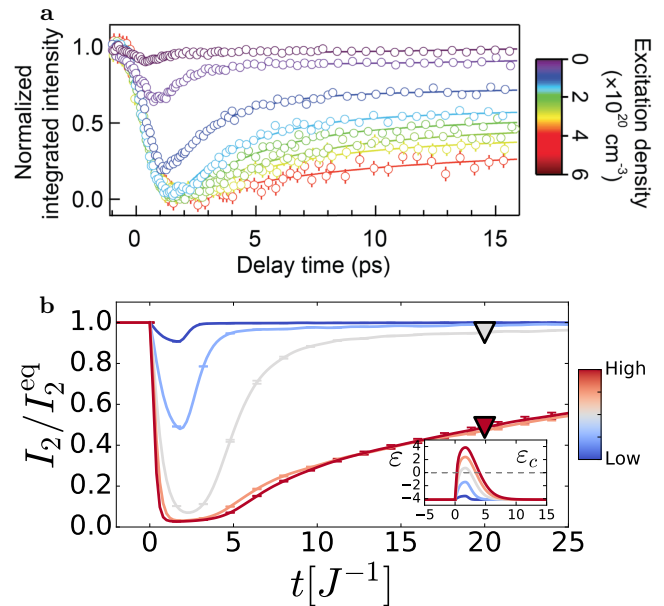


FIG. 2. (a) Time evolution of experimentally measured 2D-integrated intensity of the CDW electron diffraction peak after photo-excitation, for several laser photo-excitation densities (from Ref. [18]). (b) Numerically-calculated 2D-integrated intensity $I_2 \equiv \sum_{k_x, k_y} |\psi(k_x, k_y, 0)|^2$ tracking the ordering in the system [see Eq. (6)] as a function of time for different quench intensities. The color of the curves encodes different quench intensities as indicated on the colorbar. Each numerical data point represents the average of 40 quench realizations, and the error bars represent the statistical uncertainty associated with this average. Inset: Variation of the energy density during quenches. Horizontal line marks critical energy density ε_c , see Fig. 3(a), above which the order is destroyed.

a time-reversible Hamiltonian dynamics, while the former involves dissipative coupling with the electronic subsystem and with the rest of the lattice degrees of freedom. Yet, both a three-dimensional DGPE lattice and a three-dimensional CDW system exhibit a spontaneous symmetry breaking transition into a $U(1)$ -ordered state. Since we are primarily interested in the phase ordering dynamics associated with the formation of topological defects over larger spatial scales, it can be reasonably expected that the detailed character of the thermal bath inducing the phase fluctuations is not crucial, and, therefore, the thermal bath of the real CDW system can be efficiently replaced by the bath associated with the microcanonical thermalizing dynamics of the DGPE lattice.

To connect the CDW dynamics and the DGPE, we divide the crystal lattice into cells of sizes $l_x \times l_y \times l_z$, where l_x , l_y , and l_z are of the order of the CDW coherence lengths for the respective directions. Each cell is represented by a single site of the cubic DGPE lattice. The modelling is classical, since, for large enough cells, the quantum fluctuations can be neglected. The mapping

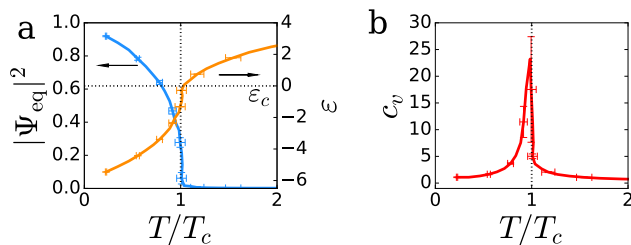


FIG. 3. Temperature dependence of various parameters for the 3D DGPE lattice: (a) the equilibrium order parameter $|\Psi_{\text{eq}}|^2$ and the energy density ε , (b) specific heat c_v .

is achieved by associating the DGPE lattice variable ψ_j with the average of the CDW order parameter over the CDW cell around position \mathbf{r}_j :

$$\psi_j \sim \left\langle u(\mathbf{r}) e^{i\phi(\mathbf{r})} \right\rangle_{j^{\text{th}} \text{ cell}}. \quad (2)$$

The time evolution of ψ_j is to be modelled by the DGPE on a cubic lattice:

$$i \frac{d\psi_j}{dt} = -J \sum_{k \in \text{NN}(j)} \psi_k + U |\psi_j|^2 \psi_j, \quad (3)$$

where the summation over k runs through all nearest-neighbors $\text{NN}(j)$ of site j , coefficient J is the “hopping” parameter and U is the interaction parameter. The lattice has V sites. In the simulations, the typical lattice dimensions were $50 \times 50 \times 50$. DGPE conserves the total energy of the lattice $E \equiv \sum_j \left(-J \sum_{k \in \text{NN}(j)} \psi_k \psi_j^* + \frac{U}{2} |\psi_j|^4 \right)$ as well as the “total norm” $N \equiv \sum_j |\psi_j|^2$. We also define the energy density $\varepsilon \equiv E/V$ and the “norm density” $n \equiv N/V$. The character of the DGPE solutions is determined by the dimensionless parameter $g \equiv Un/J$, which, for the reasons explained later, was chosen to be equal to 10. Below, except for the period of quench, we simulate an isolated DGPE lattice, which, when perturbed, is observed to exhibit dynamic thermalization to a microcanonical temperature T that was determined numerically as in Ref. [30, 31]. The computed temperature is a monotonic function of ε . For $g = 10$, the DGPE exhibits a spontaneous symmetry breaking transition at the critical temperature $T_c \approx 1.92Jn$ into low-temperature ordered state characterised by the $U(1)$ order parameter $\Psi(t) = |\Psi(t)| e^{i\phi(t)} \equiv \frac{1}{\sqrt{N}} \sum_j \psi_j(t)$. In equilibrium, $|\Psi| = |\Psi_{\text{eq}}(T)|$, where $|\Psi_{\text{eq}}(T)|$ is a decreasing function of T for $T < T_c$, vanishing above T_c . Both $\varepsilon(T)$ and $|\Psi_{\text{eq}}|^2(T)$ are plotted in Fig. 3(a). The heat capacity $c_v(T) \equiv d\varepsilon/dT$ is shown in Fig. 3(b); it exhibits a very recognizable λ -point at $T = T_c$ corresponding to $\varepsilon = \varepsilon_c$.

Parameters. — To finalize the mapping, we provide the order-of-magnitude estimates for the three parameters of the cubic DGPE lattice, namely, J , n , and U .

Since the CDW coherent domains are supposed to be larger than the crystal unit cell, the CDW phase dynamics should occur at typical frequencies smaller than the Debye frequency Ω_D . Hence, the parameter J , which determines the characteristic frequency of the DGPE dynamics, can be roughly estimated as

$$J = \Omega_D \frac{a}{l}, \quad (4)$$

where $a \equiv (a_x a_y a_z)^{1/3}$ is the geometrical average of the crystal lattice periods a_x , a_y , and a_z , and $l \equiv (l_x l_y l_z)^{1/3}$ is the geometrical average of the CDW coherence lengths l_x , l_y , and l_z . We use the mean-field theory [32], which is supposed to be rather crude for LaTe_3 , to make the order-of-magnitude estimate $l = \hbar v_F / (1.76\pi k_B T_c)$, where $v_F = 2\varepsilon_F/p_F$ is the Fermi velocity, and T_c is the CDW phase transition temperature. Thus $\varepsilon_F \approx 1.5$ eV [33], $p_F \approx \frac{3\pi}{8} \frac{\hbar}{a}$, $T_c \sim 700$ K. As a result, we get $l \sim 6a$. Inserting this together with $\Omega_D \sim 4$ THz into Eq.(4) gives $J \sim 4$ ps $^{-1}$.

The typical value for n can be derived from the fact that, at the critical temperature, the hopping energy is of order of the thermal energy $Jn \sim k_B T_c$. Thus:

$$n \sim \frac{k_B T_c}{J} \sim \hbar \frac{T_c}{T_D} \frac{l}{a}. \quad (5)$$

At the last step, we replaced $\hbar\Omega_D$ in Eq.(4) with $k_B T_D$, where $T_D \sim 200$ K is the Debye temperature for LaTe_3 [34]. Thus $n/\hbar \sim 20$, which is consistent with the classical character of our modelling.

Parameter U can be determined by matching the speed of phasons, c_{ph} with the speed of low-frequency excitations of the DGPE lattice: $c_{\text{ph}} = l\sqrt{2JU}n$ [35]. In turn, c_{ph} can be crudely estimated as the speed of sound [36]. It is further shown in [35] that, under these assumptions, $U \sim 10 \frac{l}{n}$. Therefore, our simulations were done with $g = Un/J = 10$.

Simulations of non-equilibrium quenches. — According to Ref. [19], the energy deposited by the laser pulse into LaTe_3 is first absorbed by the electrons, then transferred partially to the “hot phonons”, drastically increasing their temperature and thereby melting the CDW order. After that, the energy of the hot phonons is transferred to the rest of the phonons, which have significantly larger specific heat. This brings the overall temperature of the system to nearly the same temperature as the one before the pulse. The phase degrees of freedom we aim at describing with the help of the DGPE are supposed to belong to hot phonons. Therefore, we model the above process by first quickly pumping the energy into the DGPE lattice (heating of hot phonons by electrons) and then quickly removing the energy from the lattice (cooling of hot phonons by the energy transfer to the main phonon bath).

Technically the above scheme is implemented by temporarily adding the energy-nonconserving terms to the

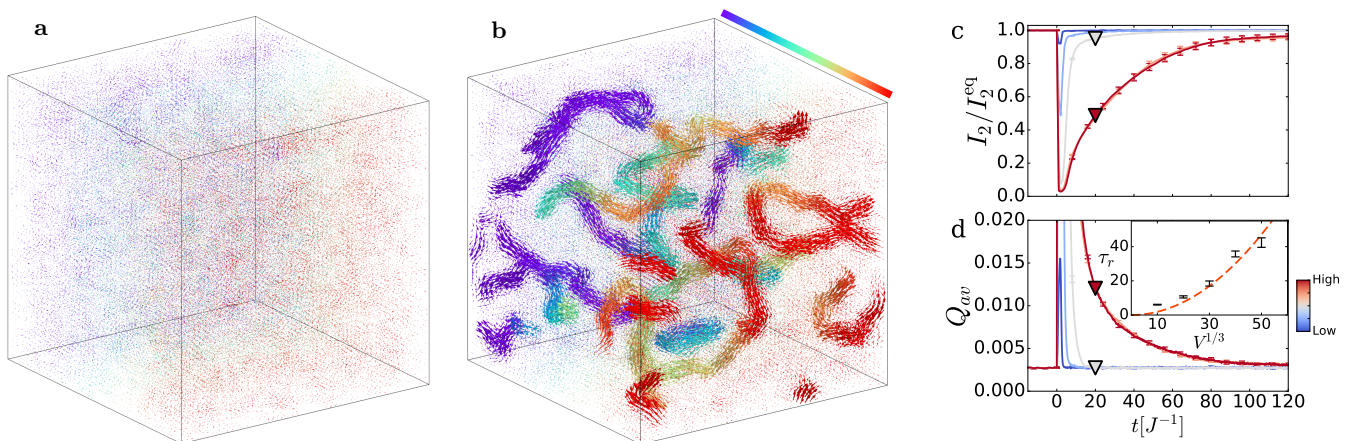


FIG. 4. (a,b) Snapshots of vorticity for two individual quenches at time $t = 20J^{-1}$: (a) weak quench, (b) strong quench, marked in panels (c,d) by gray and red triangles, respectively [also shown in Fig. 2(b)]. Vorticity \mathbf{w}_j is depicted by (colored) arrows whose length is proportional to $|\mathbf{w}_j|$ (see the text). For the visualization purposes, we apply a smoothing filter to \mathbf{w}_j : at site j we plot \mathbf{w}_j averaged over 9 sites comprising a cube with side 3 encompassing site j . The arrow color represents the position along one of the lattice axes, as shown by the color bar. In (a) these arrows are visible as mere dots due to smallness of $|\mathbf{w}_j|$. In (b) longer and hence brighter arrows merge into distinctly visible worm-like bundles revealing vortex cores. Vortex lines penetrating the entire system are clearly seen for the stronger quench. (Further snapshots of vorticity for the later times of the stronger quench can be found in the Supplement [35].) (c,d) Correlation between vorticity and the slowing down of the order recovery for the simulated 3D DGPE lattice. (c) the 2D-integrated intensity $I_2(t)$, same as Fig. 2(b) but over a longer time interval; (d) the average vorticity $Q_{av}(t)$. The color-coding and the statistical ensemble behind the sampling are used the same as in Fig. 2(b). (d, inset) Dependence of the order parameter recovery time τ_r on the linear lattice size $V^{1/3}$.

right-hand-side of Eq. (3) as explained in Refs. [31, 35, 37]. We simulated a set of quenches starting from the equilibrium state at $T \approx 0.62T_c$ and then using varying amounts of energy deposited to and then removed from the system, and averaged over 40 random initial conditions, thermalized before the quench for $t = 600J^{-1}$ [35]. The time dependencies of energy during the quenches is shown in the inset of Fig. 2(b). These quenches imitated the experimental laser pulses of different fluences used to produce the experimental plots in Fig. 2(a).

To compare our simulation against the diffraction experiment [18], we define the two-dimensional integrated spectral weight $I_2(t)$ by the following equality

$$I_2 = \sum_{k_x, k_y} |\psi(k_x, k_y, 0)|^2, \quad (6)$$

where $\psi(\mathbf{k}) = V^{-1} \sum_j \psi_j e^{i\mathbf{k} \cdot \mathbf{r}_j}$ is the Fourier transform of ψ_j . Summation in Eq. (6) runs over quantized momentum projections $k_{x,y}$ lying in the Brillouin zone, while $k_z = 0$. Definition (6) mimics the 2D-integrated diffraction intensity measured experimentally in Ref. [18], see Fig. 2(a). The square of the order parameter amplitude $|\Psi|^2$ is the largest contributing term in the sum (6). However, $I_2 > |\Psi|^2$ since shorter-range order fluctuations enhance I_2 relative to $|\Psi|^2$. Thus, one can think of I_2 as a quantity tracking both long-range and short-range correlations in the DGPE system. We have further verified [35] that $I_2(t)$ is proportional to the correlation length of the CDW order, $l_c(t)$, as anticipated in Refs. [18, 19].

The main panel of Fig. 2(b), presents $I_2(t)$ before, during and after the quench. The comparison between the simulation and the experiment reveals a remarkable agreement: At small intensities of the quench, the spectral intensity quickly recovers its pre-quench equilibrium value on the time scale comparable to the duration of the quench itself. As the quench intensity grows, the character of the dynamics undergoes a qualitative change: I_2 drops to zero and stays low for finite time interval. This happens when, during the quench, the energy crosses the critical value ε_c associated with the phase transition and indicated by the dashed line in the inset of Fig. 2(b). Most importantly, the post-quench recovery is extremely slow: the corresponding curves visually split away from the curves representing weaker quenches.

Topological defects. — Here we investigate the possible connection between the slowdown of the order recovery and the dynamics of topological defects. For 3D DGPE systems with periodic boundary conditions, the topological defects form closed-loop vortices [38]. In this respect, the 3D DGPE model is similar to the three-dimensional $O(2)$, $U(1)$ and XY-models, where the percolation of vortex loops is responsible for a phase transition and a symmetry breaking [39–41].

To monitor the local topological charge (vorticity), we define the dual lattice by translating the original lattice by vector $(1/2, 1/2, 1/2)$. Each of the sites of the dual lattice is thus surrounded by 8 sites of the original lattice, which form 6 square plaquettes.

As an indicator of vorticity we use the finite-difference counterpart \mathbf{w}_j of the continuous curl of the current $(\nabla \times \mathbf{v}_s)_j$, where $\mathbf{v}_s = -i(\psi^* \nabla \psi - \psi \nabla \psi^*)$. The numerical calculation of \mathbf{w}_j for each dual lattice site is based on the fourth-order finite differentiation scheme for each first-order derivative $(df(x)/dx)_j = (f_{j+2} - 8f_{j+1} + 8f_{j-1} - f_{j-2})/12$.

In Fig. 4(a,b), we provide a space-resolved snapshots of the vorticity field \mathbf{w}_j generated in the course of the quenches shown in Fig. 2(b). The snapshots correspond to the two states marked in Fig. 2(b) by red and gray triangles. In principle, each site of the dual lattice has a non-zero vorticity \mathbf{w}_j , which is the consequence of the discreteness of the lattice field. However, in the absence of a real vortex, such a vorticity is very small and does not form any line pattern, while the presence of a vortex is indicated by the large values of \mathbf{w}_j showing the vortex core as a colored “tube” extended through the lattice. Fig. 4(a) illustrates a weak quench, for which the order (quantified by I_2) recovers quickly. One can see that the system does not exhibit any colored tube indicative of a vortex. For more intensive quenches, on the contrary, one can observe vortex tubes percolating through large volumes of the system and forming clearly identifiable large vortex loops, see Fig. 4(b) (see also Fig. S.7(a-c) and the video in the supplemental material [35]). As one can see, for example, in the video, these loops initially form an entangled network. The crossings of the loop lines then lead to smaller loops separating from this network and collapsing, while one large loop spreading over most of the lattice is eventually being formed. The time required for that last loop to shrink and collapse is what determines the time scale of the order recovery in Fig. 2(b).

We also introduce an auxiliary binary vorticity variable Q_j for each dual lattice site. As explained in the Supplement [35], it is defined such that $Q_j = 1$, if at least one of the 6 adjacent original-lattice plaquettes has non-zero vorticity; otherwise $Q_j = 0$. Finally, we define the average vorticity for the entire system as $Q_{av} = \frac{1}{V} \sum_j Q_j$.

In Figs. 4(c,d), we present further evidence that the relaxation of vorticity $Q_{av}(t)$ in the simulated system is directly correlated with the order recovery after a quench. There one can see that the strong quenches exhibiting the slowdown of the I_2 recovery are accompanied by a pronounced slowly relaxing tails of $Q_{av}(t)$.

In Fig. 4(c, inset), we show that the order parameter recovery τ_r , defined as the time to reach 75% of the initial equilibrium value of $|\Psi|^2$ for the strongest quench, grows with the lattice volume (number of lattice sites) V . The simulations are consistent with the scaling $\tau_r \propto V^{2/3}$. We have not attempted to derive this power law. Yet, the growth of τ_r with the lattice size as such indicates that the recovery of the order is contingent on the disappearance of the extensive vortex loops that penetrate the entire system and need to drift by the distances of the order of the lattice size before they annihilate.

Conclusions — In conclusion, our direct simulations of the DGPE lattice with a CDW-like form of the order parameter are consistent with the conjecture of Ref. [18] that the observed slowdown of the recovery of the CDW order after laser-induced melting is due to the emergence and then slow disappearance of topological defects in the order parameter texture. We were able to numerically monitor the vorticity in the system and thereby establish the correlation between the relaxation of vorticity and the recovery of the order. In a broader context, our investigation illustrates the viability of using DGPE for simulating the CDW dynamics even though DGPE as such was historically introduced to describe superfluid systems.

Code availability — The source code is published in a GitHub repository [42].

Acknowledgments. — This work was supported by a grant of the Russian Science Foundation (Project No. 17-12-01587). The work at MIT was mainly funded by the U.S. Department of Energy, BES DMSE (data taking and analysis) and the Gordon and Betty Moore Foundation’s EPiQS Initiative grant GBMF9459 (instrumentation).

* atarkhov@bwh.harvard.edu

† boris.fine@uni-leipzig.de

- [1] V. Berezinsky, Zh. Eksp. Teor. Fiz. **32**, 493 (1970).
- [2] V. Berezinsky, Zh. Eksp. Teor. Fiz. **61**, 610 (1972).
- [3] J. M. Kosterlitz and D. Thouless, J. Phys. C: Solid State Phys. **5**, L124 (1972).
- [4] B. Svistunov, J. Moscow Phys. Soc **1**, 373 (1991).
- [5] Y. M. Kagan, B. Svistunov, and G. Shlyapnikov, JETP **75**, 387 (1992).
- [6] Y. Kagan and B. Svistunov, Zh. Eksp. Teor. Fiz **105**, 353 (1994).
- [7] N. G. Berloff and B. V. Svistunov, Phys. Rev. A **66**, 013603 (2002).
- [8] H. Yoshino, K. Hukushima, and H. Takayama, Phys. Rev. B **66**, 064431 (2002).
- [9] T. C. Proctor, D. A. Garanin, and E. M. Chudnovsky, Phys. Rev. Lett. **112**, 097201 (2014).
- [10] D. A. Garanin and E. M. Chudnovsky, The European Physical Journal B **88**, 81 (2015).
- [11] M. Kobayashi and L. F. Cugliandolo, Phys. Rev. E **94**, 062146 (2016).
- [12] M. Kumar, S. Chatterjee, R. Paul, and S. Puri, Phys. Rev. E **96**, 042127 (2017).
- [13] M. Vasin and V. Vinokur, Physica A **525**, 1161 (2019).
- [14] T. W. Kibble, J. Phys. A: Math. Gen. **9**, 1387 (1976).
- [15] T. W. Kibble, Phys. Rep. **67**, 183 (1980).
- [16] W. H. Zurek, Nature **317**, 505 (1985).
- [17] W. H. Zurek, Phys. Rep. **276**, 177 (1996).
- [18] A. Zong, A. Kogar, Y.-Q. Bie, T. Rohwer, C. Lee, E. Baldini, E. Ergeçen, M. B. Yilmaz, B. Freelon, E. J. Sie, H. Zhou, J. Straquadine, P. Walmsley, P. E. Dolgirev, A. V. Rozhkov, I. R. Fisher, P. Jarillo-Herrero, B. V. Fine, and N. Gedik, Nat. Phys. **15**, 27 (2019).
- [19] P. E. Dolgirev, A. V. Rozhkov, A. Zong, A. Kogar,

- N. Gedik, and B. V. Fine, Phys. Rev. B **101**, 054203 (2020).
- [20] M. Trigo, P. Giraldo-Gallo, J. N. Clark, M. E. Kozina, T. Henighan, M. P. Jiang, M. Chollet, I. R. Fisher, J. M. Glowina, T. Katayama, P. S. Kirchmann, D. Leuenberger, H. Liu, D. A. Reis, Z. X. Shen, and D. Zhu, Phys. Rev. B **103**, 054109 (2021).
- [21] S. Wandel, F. Boschini, E. H. da Silva Neto, L. Shen, M. X. Na, S. Zohar, Y. Wang, G. B. Welch, M. H. Seaberg, J. D. Koralek, G. L. Dakovski, W. Hettel, M.-F. Lin, S. P. Moeller, W. F. Schlotter, A. H. Reid, M. P. Minitti, T. Boyle, F. He, R. Sutarto, R. Liang, D. Bonn, W. Hardy, R. A. Kaindl, D. G. Hawthorn, J. S. Lee, A. F. Kemper, A. Damascelli, C. Giannetti, J. J. Turner, and G. Coslovich, “Light-enhanced charge density wave coherence in a high-temperature superconductor,” (2020), arXiv:arxiv:2003.04224 [cond-mat.supr-con].
- [22] A. Kogar, A. Zong, P. E. Dolgirev, X. Shen, J. Straquadine, Y.-Q. Bie, X. Wang, T. Rohwer, I.-C. Tung, Y. Yang, R. Li, J. Yang, S. Weathersby, S. Park, M. E. Kozina, E. J. Sie, H. Wen, P. Jarillo-Herrero, I. R. Fisher, X. Wang, and N. Gedik, Nat. Phys. **16**, 159 (2020).
- [23] D. Mihailovic, Appl. Sci. **9** (2019), 10.3390/app9050890.
- [24] S. Vogelgesang, G. Storeck, J. Horstmann, T. Diekmann, M. Sivis, S. Schramm, K. Rosnagel, S. Schäfer, and C. Ropers, Nature Physics **14**, 184 (2018).
- [25] S. Duan, Y. Cheng, W. Xia, Y. Yang, C. Xu, F. Qi, C. Huang, T. Tang, Y. Guo, W. Luo, *et al.*, Nature **595**, 239 (2021).
- [26] G. Storeck, J. G. Horstmann, T. Diekmann, S. Vogelgesang, G. von Witte, S. V. Yalunin, K. Rosnagel, and C. Ropers, Structural Dynamics **7**, 034304 (2020), <https://doi.org/10.1063/4.0000018>.
- [27] A. Zong, A. Kogar, and N. Gedik, MRS Bull. **46**, 720 (2021).
- [28] J. Maklar, Y. W. Windsor, C. W. Nicholson, M. Puppin, P. Walmsley, V. Esposito, M. Porer, J. Rittmann, D. Leuenberger, M. Kubli, M. Savoini, E. Abreu, S. L. Johnson, P. Beaud, G. Ingold, U. Staub, I. R. Fisher, R. Ernstorfer, M. Wolf, and L. Rettig, Nat. Commun. **12**, 2499 (2021).
- [29] A. Zong, P. E. Dolgirev, A. Kogar, E. Ergeçen, M. B. Yilmaz, Y.-Q. Bie, T. Rohwer, I.-C. Tung, J. Straquadine, X. Wang, Y. Yang, X. Shen, R. Li, J. Yang, S. Park, M. C. Hoffmann, B. K. Ofori-Okai, M. E. Kozina, H. Wen, X. Wang, I. R. Fisher, P. Jarillo-Herrero, and N. Gedik, Phys. Rev. Lett. **123**, 097601 (2019).
- [30] A. S. de Wijn, B. Hess, and B. V. Fine, Phys. Rev. E **92**, 062929 (2015).
- [31] A. E. Tarkhov, *Ergodization dynamics of the Gross-Pitaevskii equation on a lattice*, Ph.D. thesis, Skolkovo Institute of Science and Technology (2020).
- [32] G. Gruner, *Density waves in solids* (CRC press, 2018).
- [33] H. Yao, J. A. Robertson, E.-A. Kim, and S. A. Kivelson, Phys. Rev. B **74**, 245126 (2006).
- [34] N. Ru and I. Fisher, Phys. Rev. B **73**, 033101 (2006).
- [35] Supplemental Material to this paper.
- [36] M. E. Manley, P. J. Stonaha, D. L. Abernathy, S. Chi, R. Sahul, R. P. Hermann, and J. D. Budai, Nat. Commun. **9**, 1 (2018).
- [37] A. E. Tarkhov, A. Rozhkov, and B. V. Fine, arXiv preprint arXiv:2109.00961 (2021).
- [38] F. Rojas, S. Puri, and A. Bray, J. Phys. A: Math. Gen. **34**, 3985 (2001).
- [39] A. Hulsebos, Nuclear Physics B-Proceedings Supplements **34**, 695 (1994).
- [40] K. Kajantie, M. Laine, T. Neuhaus, A. Rajantie, and K. Rummukainen, Phys. Lett. B **482**, 114 (2000).
- [41] G. Kohring, R. E. Shrock, and P. Wills, Phys. Rev. Lett. **57**, 1358 (1986).
- [42] The code is published in a GitHub repository at <https://github.com/TarkhovAndrei/DGPE>.
- [43] H. H. Rugh, Phys. Rev. Lett. **78**, 772 (1997).
- [44] H. H. Rugh, J. Phys. A: Math. Gen. **31**, 7761 (1998).
- [45] A. Kamaletdinov and N. G. Berloff, “Quantized vortices mediated annealing,” (2021), arXiv:2109.05867 [cond-mat.dis-nn].

SUPPLEMENTAL MATERIAL

S.I. Details of the experiment of Ref.[18]

Here, for the convenience of the readers, we provide additional details of the experiment of Ref.[18].

The material studied, LaTe_3 , has a layered crystal structure consisting of alternating Te bilayers and LaTe layers. The critical temperature of the CDW transition in LaTe_3 is about 700 K. The CDW is localized primarily in the Te bilayers.

In the experiment of Ref.[18], femtosecond laser pulses were applied to LaTe_3 and then the CDW response was probed by (i) optical reflectivity measurements, (ii) time-resolved angle-resolved photoemission spectroscopy and (iii) the ultrafast electron diffraction. Fig. 2(a) of the main text shows the results for the latter technique, namely, the 2D-integrated intensity, I_2 , of the CDW electron diffraction peak is plotted as a function of delay time for various laser pulse fluences. The peak intensity is integrated for the two in-plane wave-vector projections. The intensity is interpreted as being proportional to the square of the CDW order-parameter multiplied by the CDW correlation length for the out-of-plane direction (the one perpendicular to the Te layers).

By examining the time evolution of the width of the CDW peak, the authors Ref.[18] provided indirect evidence that the slow recovery of the intensity of the CDW diffraction peak seen in Fig. 2(a) is caused by the emergence of topological defects of the CDW order, followed by their subsequent slow annihilation. Even though such a scenario is rather natural, no direct evidence in real space in its favor was presented.

S.II. Microcanonical thermodynamics of the DGPE lattice: Numerical aspects

Equilibrium properties

For the parameters used in the main text, the solutions of DGPE with fixed E and N were observed to exhibit the behavior consistent with the ergodic hypothesis. Namely, the right-hand-side of Eq. (S.2) computed for a given phase space trajectory and used below to define the temperature was found to converge to a value independent of the initial conditions.

To describe the statistical properties of the DGPE lattice, we use the standard definition of the microcanonical temperature:

$$\frac{1}{T} \equiv \frac{\partial S}{\partial E}, \quad (\text{S.1})$$

where $S \equiv \log W(E)$ is the microcanonical entropy, with $W(E)$ being the $(V-2)$ -dimensional volume of the energy

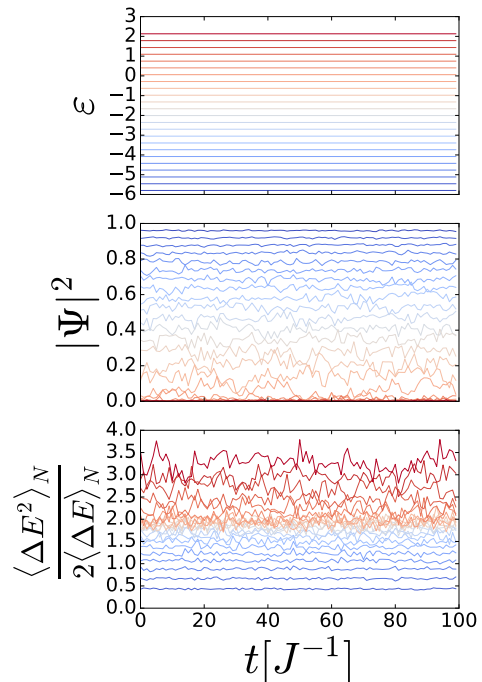


FIG. S.1. Thermalization dynamics behind Fig. 3, $V = 10^3$: energy density, order parameter and the right-hand-side of Eq. (S.2)

shell at constant N . We set the Boltzmann constant $k_B = 1$.

The direct determination of the volume $W(E)$ in the many-dimensional phase space is a computationally prohibitive task. It is, however, possible to use Monte-Carlo sampling to determine directly $\frac{1}{W(E)} \frac{dW(E)}{dE}$, which is equal to the right-hand-side of Eq.(S.1). We do this by adapting the numerical recipe developed for classical spin lattices [30] and consistent with the analytical approach of Refs. [43, 44]. The idea is based on the observation that the rate of growth of a many-dimensional energy shell is determined by the average local curvature of that shell. The latter, in turn, can be locally sampled in the vicinity of each point by introducing small isotropic random perturbations to the phase point coordinate and then computing the variance of energy fluctuations $\langle \Delta E^2 \rangle$ and the mean fluctuation $\langle \Delta E \rangle$. We note that $\langle \Delta E \rangle \neq 0$ due to the fact that, in general, there are exponentially more states above the energy shell than below it. We use the above approach with the additional constraint that the small perturbations should leave N constant. The corresponding average is denoted as $\langle \dots \rangle_N$. With such a notation, the numerically computed expression for temperature becomes

$$\frac{1}{T} = \frac{2 \langle \Delta E \rangle_N}{\langle \Delta E^2 \rangle_N}. \quad (\text{S.2})$$

In the limit $V \rightarrow \infty$, computing the averages entering

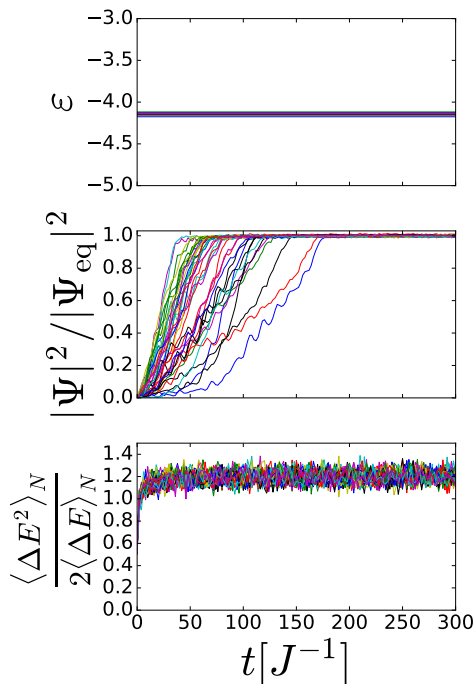


FIG. S.2. Thermalization of pre-quench states for 40 on-shell initial conditions generated by the procedure described in Section S.II with $V = 50^3$.

Eq.(S.2) in the vicinity of one randomly chosen sample point on an energy shell should be sufficient to determine the temperature. However, since our numerically simulated lattice is finite, we supplement the above procedure by the additional averaging of the right-hand-side of Eq.(S.2) over points along a randomly chosen phase space trajectory and then further over phase space trajectories with randomly chosen initial conditions.

Technically, the calculation of equilibrium properties plotted in Fig. 3 consists of the following steps:

- (i) choosing the initial configurations $\{\psi_j\}$ as a random Hilbert-space vector normalised by the condition $\sum_j |\psi_j|^2 \equiv N = V$. This state has randomly chosen phases and amplitudes, and corresponds to $\varepsilon \sim 0$ and $T \sim T_c$;
- (ii) choosing an energy value for which the temperature is to be calculated;
- (iii) activating the non-conservative term in the DGPE Eq. (S.3) with function $K \equiv \text{const}$ for a time interval sufficient to reach a desired energy value (see Section S.III);
- (iv) deactivating the non-conservative term, then calculating the conservative dynamics of the DGPE for a sufficiently long time $t = 100J^{-1}$ (see Fig. S.1);
- (v) choosing the next slightly smaller target energy value and then, starting from the thermalized state

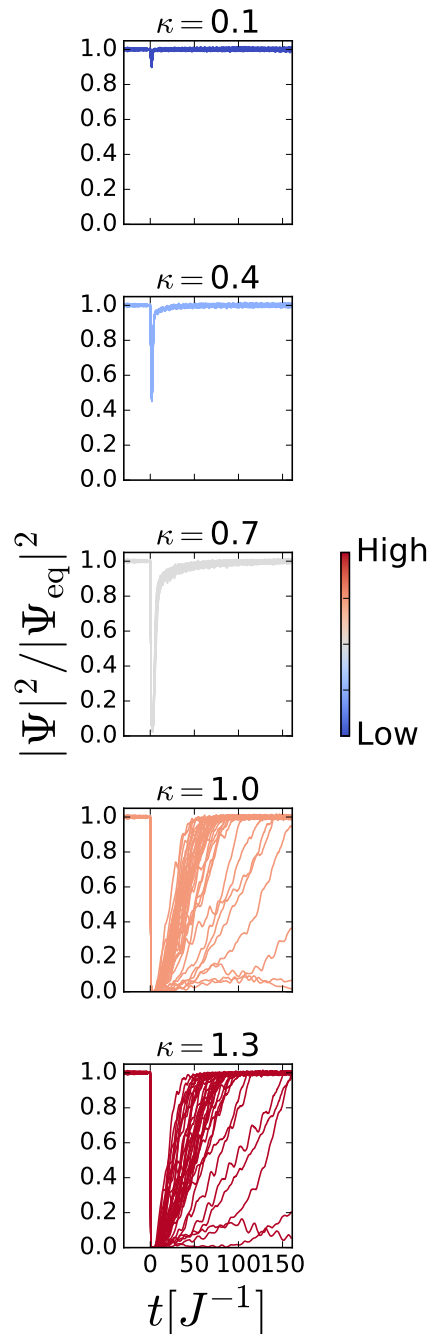


FIG. S.3. Quench realizations behind the averages plotted in Figs. 2(b) and 4(a) – 40 initial conditions, $V = 50^3$. For stronger quenches $\kappa = 1.0$ and $\kappa = 1.3$, atypical slowly relaxing solutions appear – they indicate the presence of large topological defects in the lattice.

at the final time point from the preceding step, repeating steps (ii) to (v).

The overall procedure guarantees that the DGPE lattice has enough time to thermalize at each energy shell.

Preparation of the initial state preceding the quenches.

In Fig. S.2, we illustrate the preparation of the initial thermalized state for the quenches presented in Fig. 2(b) of the main text of the paper. We start from the high-temperature state of step (i) above and then quickly drive the system to $\varepsilon = -4.1$ corresponding to $T \approx 0.62T_c$. Such a driving initially produces a strongly nonequilibrium state (in contrast to the slow preparation procedure used in the previous subsection). Then, we track the thermalization dynamics of ε , $\frac{|\Psi|^2}{|\Psi_{\text{eq}}|^2}$ and $\frac{2\langle\Delta E\rangle_N}{\langle\Delta E^2\rangle_N}$ from Eq. (S.2). We observe that the energy is conserved, the order parameter reaches its equilibrium value by $t \sim 150J^{-1}$, while the parameter $\frac{2\langle\Delta E\rangle_N}{\langle\Delta E^2\rangle_N}$ starts exhibiting the typical behavior faster, namely, after times of the order of $t \sim 10J^{-1}$. By time $t = 200J^{-1}$, all the parameters reach their equilibrium regimes independently of the initial conditions. For the quenches, presented in Fig. 2(b) of the main text, the conservative dynamics were run for $t = 600J^{-1}$, which is significantly longer than required for equilibration and thermalization. Hence, before the start of the quenches in Fig. 2(b) the system was well-thermalized, and the initial conditions for the quenches are typical for the energy shell.

S.III. Numerical implementation of the DGPE lattice quench

The quench is performed on the DGPE lattice prepared in equilibrium at $\varepsilon = -4.1$, $T/T_c \approx 0.62$. During the quench, the system's energy experiences quick rise and fall within a limited time interval. To allow for the time variation of E , we modify [31, 37, 45] DGPE by adding a non-energy-conserving term (the last one below):

$$i\frac{d\psi_j}{dt} = - \sum_{k \in \text{NN}(j)} \psi_k + \frac{Un}{J} |\psi_j|^2 \psi_j - K(t)\psi_j D_j, \quad (\text{S.3})$$

where

$$D_j = D_j^* = i \sum_{k \in \text{NN}(j)} (\psi_k^* \psi_j - \psi_k \psi_j^*), \quad (\text{S.4})$$

and the function $K(t, \kappa)$ is to be specified below. Note that Eq. (S.3), remains ‘‘gauge invariant’’ and thus conserves the norm N .

To verify the energy-nonconserving character of the added term one can use Eq. (S.3) to obtain

$$\dot{E} = -K(t) \sum_j D_j^2. \quad (\text{S.5})$$

The sign of $K(t)$ controls the increase or decrease of E : function K must be negative to heat the system, and pos-

itive to cool it. We additionally require that the energies of the system before and after the quench are identical.

All our simulated quenches use the function $K(t)$ having the following form

$$K(t) = -\theta(t) \left[\kappa \frac{\gamma_2 e^{-\gamma_2 t} - \gamma_1 e^{-\gamma_1 t}}{\gamma_2 - \gamma_1} - \theta(t - t^*) \gamma_3 \left(1 - e^{-\gamma_2(t-t^*)} \right) \frac{E(t) - E_0}{E^* - E_0} \right], \quad (\text{S.6})$$

where $\theta(t)$ is the Heaviside step-function, κ is the parameter controlling the strength of the quench (in our simulations, κ spans the range from 0.1 to 20), $\gamma_1 = 1$, $\gamma_2 = 0.3$ and $\gamma_3 = 0.01$ are numerical parameters,

$$t^* = \frac{1}{\gamma_1 - \gamma_2} \log \left(\frac{\gamma_1}{\gamma_2} \right) \quad (\text{S.7})$$

is the time at which $K(t)$ changes sign, E_0 is the pre-quench energy of the system, $E(t)$ is the energy at time t , and $E^* = E(t^*)$.

The quench is principally determined by the first term in the square brackets in Eq.(S.6) – the time-dependence of this term is shown in Fig. S.4. The second term in the square brackets is added to guarantee that the energy after the quench is equal to the initial energy E_0 .

Before the quench, the system is prepared in an equilibrium low-energy state as described in Section S.II. At the first stage of the quench the system is subjected to the fast energy increase (heating). The duration that stage is t^* . The heating is then followed by the cooling stage of duration regulated by parameters γ_2 and γ . The resulting time evolution of the energy density $\varepsilon(t)$ for various quench parameters κ is plotted in the inset of Fig. 2(b) of the main text.

For further details one can refer to the source code published in a GitHub repository [42].

S.IV. Estimate of parameter U for the DGPE lattice

In order to estimate the nonlinearity parameter U , we match the velocity of the phasons propagating within the real CDW system and the velocity of acoustic excitations calculated theoretically for the DGPE model. To perform the desired calculation, we treat phasons as weak perturbations distorting spatially homogeneous zero-temperature solution $\Psi_0(t)$. Within such an approach, the original DGPE variables ψ_j should be expressed as the sum $\psi_j(t) = \Psi_0(t) + \xi_j(t)$, where variables $\xi_j(t)$ are small. The DGPE now reads

$$i\dot{\Psi}_0 + i\dot{\xi}_j = -2dJ\Psi_0 - J \sum_{m \in \text{NN}(j)} \xi_m + U |\Psi_0 + \xi_j|^2 (\Psi_0 + \xi_j). \quad (\text{S.8})$$

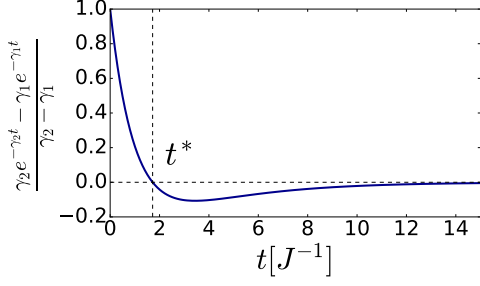


FIG. S.4. The principal factor in the first term in Eq. (S.6) as a function of time.

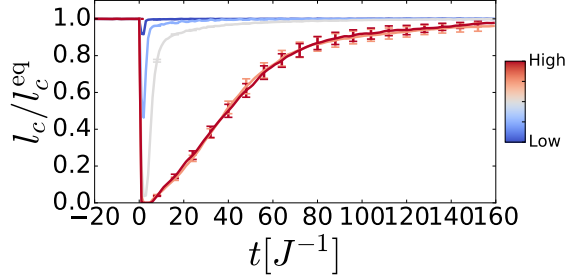


FIG. S.5. Time dependence of the correlation length for the quench illustrated in Fig. 2(b) and Fig. 4(c).

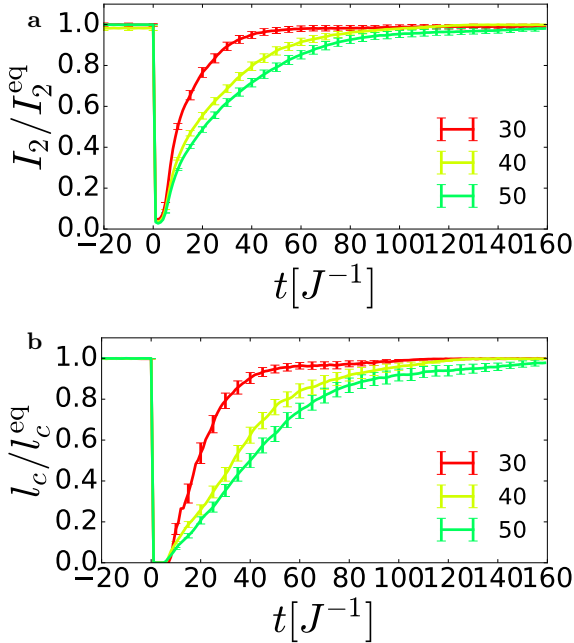


FIG. S.6. System size scaling for the time evolution of (a) the theoretically computed post-quench recovery, I_2 , and (b) the correlation length, l_c . The color of the curves represents different system sizes.

Neglecting all terms containing ξ , we derive that the unperturbed zero-temperature solution $\Psi_0(t)$ must satisfy

$$i\dot{\Psi}_0 = -2dJ\Psi_0 + U|\Psi_0|^2\Psi_0. \quad (\text{S.9})$$

The solution to the latter equation can be trivially found

$$\Psi_0(t) = \sqrt{n_0} \exp(-it\mu), \quad (\text{S.10})$$

where $n_0 = |\Psi_0|^2$ and the ‘‘chemical potential’’ $\mu = -6J + Un_0$.

When the deviations from the homogeneous zero-temperature solution (S.10) are small ($|\xi| \ll \sqrt{n_0}$), it is permissible to keep only the leading-order terms in Eq. (S.8). This allows us to derive the following linear differential equation

$$i\dot{\zeta}_j = -J \sum_{m \in \text{NN}(j)} \zeta_m - \mu\zeta_j + U(2n_0\zeta_j + n_0\zeta_j^*). \quad (\text{S.11})$$

The new dynamical variables ζ_j introduced in this equation are connected to ξ_j by the relation $\xi_j = \zeta_j e^{-it\mu}$.

In Fourier space Eq. (S.11) becomes

$$i\dot{\zeta}_{\mathbf{k}} = (\varepsilon_{\mathbf{k}} - \mu + 2Un_0)\zeta_{\mathbf{k}} + Un_0\zeta_{-\mathbf{k}}^*, \quad (\text{S.12})$$

where $\varepsilon_{\mathbf{k}}$ is defined as

$$\varepsilon_{\mathbf{k}} = -2J[\cos(k_x l) + \cos(k_y l) + \cos(k_z l)]. \quad (\text{S.13})$$

Since Eq. (S.12) couples $\zeta_{\mathbf{k}}$ and $\zeta_{-\mathbf{k}}^*$, we need to solve Eq. (S.12) together with the equation for $\zeta_{-\mathbf{k}}^*$, which reads

$$-i\dot{\zeta}_{-\mathbf{k}}^* = (\varepsilon_{\mathbf{k}} - \mu + 2Un_0)\zeta_{-\mathbf{k}}^* + Un_0\zeta_{\mathbf{k}}. \quad (\text{S.14})$$

Solving the system of equations (S.12) and (S.14), we find the spectrum of excitations $\omega_{\mathbf{k}}$ for the DGPE lattice. Frequencies $\omega_{\mathbf{k}}$ satisfy

$$\det \begin{pmatrix} \omega_{\mathbf{k}} - \varepsilon_{\mathbf{k}} + \mu - 2Un_0 & -Un_0 \\ -Un_0 & -\omega_{\mathbf{k}} - \varepsilon_{\mathbf{k}} + \mu - 2Un_0 \end{pmatrix} = 0. \quad (\text{S.15})$$

The positive branch of the resulting dispersion relation is

$$\omega_{\mathbf{k}} = \sqrt{(6J + \varepsilon_{\mathbf{k}} + Un_0)^2 - U^2 n_0^2}. \quad (\text{S.16})$$

When $l|\mathbf{k}| \ll 1$, it can be further approximated as

$$\omega_{\mathbf{k}} \approx \sqrt{(Jl^2 \mathbf{k}^2)^2 + 2l^2 JUn_0 \mathbf{k}^2} \approx c_{\text{ex}} |\mathbf{k}|, \quad (\text{S.17})$$

where $c_{\text{ex}} = l\sqrt{2JUn_0}$ is the speed of the acoustic excitations.

We map the DGPE onto the CDW dynamics by equating c_{ex} with the speed of CDW phasons c_{ph} , thereby arriving to the relation:

$$c_{\text{ph}} = l\sqrt{2JUn_0} \quad (\text{S.18})$$

used in the main text.

We then use Eq. (S.18) to estimate the DGPE nonlinearity term U as follows:

$$U = \frac{J}{2n} \left(\frac{c_{\text{ph}}}{Jl} \right)^2 = \frac{J}{2n} \left(\frac{c_{\text{ph}}}{\Omega_{\text{D}} a} \right)^2 = (6\pi^2)^{2/3} \frac{J}{2n} \left(\frac{c_{\text{ph}}}{c_s} \right)^2, \quad (\text{S.19})$$

where $c_s \sim (6\pi^2)^{-1/3} \Omega_{\text{D}} a$ is the speed of sound.

As a further crude estimate, we now use $c_{\text{ph}} \sim c_s$, thereby obtaining $U \sim 10 \frac{J}{n}$. (Ref. [36] showed that the CDW phason velocity can be 2.8–4.3 the sound velocity.)

S.V. Definition of the vorticity variable Q_j

In order to define the vorticity variable Q_j , we first introduce the auxiliary variable q_p for each plaquette surrounding the dual site j as follows: (i) The DGPE lattice variables are parameterised as $\psi_j = |\psi_j| \exp(i\phi_j)$. (ii) For a given plaquette consisting of vertices labelled as 1, 2, 3 and 4, we define

$$q_p = \frac{1}{2\pi} [(\phi_2 - \phi_1)|_{[-\pi, \pi)} + (\phi_3 - \phi_2)|_{[-\pi, \pi)} + (\phi_4 - \phi_3)|_{[-\pi, \pi)} + (\phi_1 - \phi_4)|_{[-\pi, \pi)}], \quad (\text{S.20})$$

where the notation $(\dots)|_{[-\pi, \pi)}$ indicates that the phase differences are “backfolded” into the interval $[-\pi, \pi)$. The variable q_p can take only three possible values $-1, 0$ and 1 . We then define the variable Q_j such that $Q_j = 0$ if all adjacent plaquettes have $q_p = 0$, and $Q_j = 1$ otherwise.

S.VI. Relation between I_2 and the correlation length of the CDW order

The δ -function peak due to the CDW order is known to be broadened by the presence of topological defects, which make the peak to acquire a finite width. The intensity of the δ -peak is then spread over a range of small wavevectors q , which in the real space then leads to a finite correlation length of the CDW order. The same is supposed to be true in our simulations around the ordering vector at $q = 0$.

We have found empirically, that the low- q intensity in the presence of vortices scales as

$$W(q) = A/q^2. \quad (\text{S.21})$$

Such a scaling is naturally expected given that the low- q fluctuations should be associated with the sound waves of a vortex liquid with dispersion $\omega \propto q$. The equilibrium thermal amplitude of each mode a_q is supposed to obey the relation $a_q^2 \omega^2 = T$, from which Eq.(S.21) follows given also that $W(q) \propto a_q^2$.

The singular character of the above shape precludes one from defining the correlation length from the half-width of the peak at half maximum. Instead, we define the correlation length as

$$l_c = \frac{\pi}{q_0}, \quad (\text{S.22})$$

where q_0 is the upper cutoff value for $W(q)$ given by Eq.(S.21). In turn, the value of q_0 can be estimated in the isotropic thermodynamic limit from the sum rule

$$|\Psi_0|^2 = \int_0^{q_0} W(q) 4\pi q^2 dq, \quad (\text{S.23})$$

which is just an expression of the fact that the intensity of the perfect long-range order $|\Psi_0|^2$ becomes redistributed over small q due to the presence of the topological defects.

Equations (S.21), (S.22) and (S.23) lead to

$$l_c = \frac{4\pi^2 A}{|\Psi_0|^2}. \quad (\text{S.24})$$

In our simulations, we track $W(q)$ after a quench as a function of time, fit the low- q part using Eq.(S.21) and, thereby, obtain the value of the constant A as a function of time. The latter is then substituted to Eq.(S.24) to obtain the time dependence of the correlation length.

The resulted time dependencies of l_c are plotted for different quench strengths in Fig. S.5 and for different lattice sizes in Fig. S.6(b). The comparison of these plots with Figs. 4(c) and S.6(a) respectively illustrates, that, as anticipated in Refs. [18, 19], the behavior of I_2 very closely tracks the behavior of l_c .

S.VII. Additional snapshots of vorticity after a quench

In Fig. S.7, we present three supplemental snapshots of vorticity for a strong quench from Fig. 4(b) at times $t = 25, 30$ and $35J^{-1}$. The subsequent dynamics of vortices can be observed from these snapshots. The vortices tend to decrease their size, and slowly collapse and disappear.

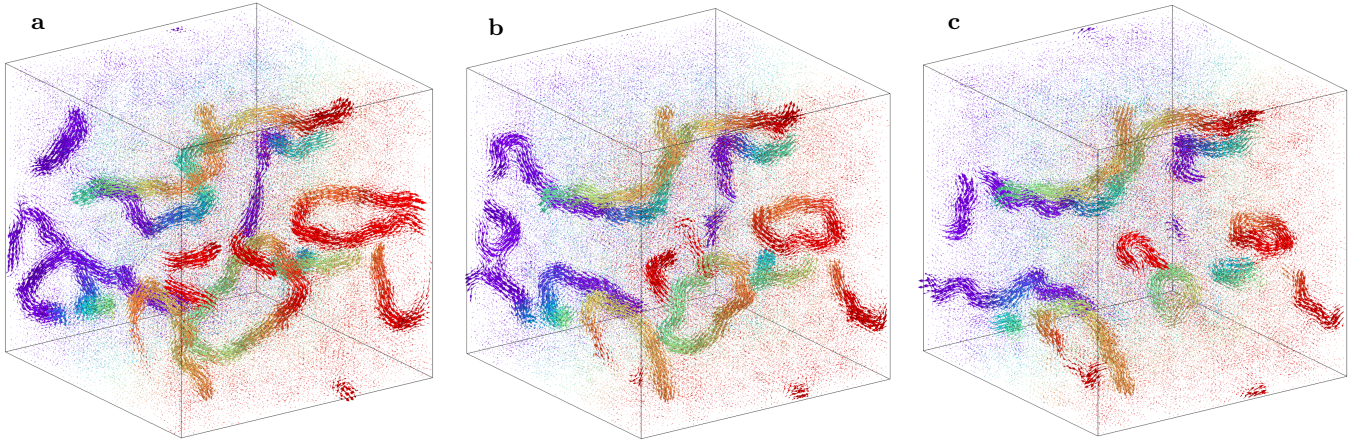


FIG. S.7. Dynamics of vortices. Snapshots of vorticity for a strong quench from Fig. 4(b) at times (a) $t = 25J^{-1}$, (b) $t = 30J^{-1}$ and (c) $t = 35J^{-1}$.